Green Chemistry

PAPER

One-step synthesis of mesoporous platinum/titania nanocomposites as photocatalyst with enhanced photocatalytic activity for methanol oxidation

Adel A. Ismail*[a] and Detlef W. Bahnemann[b]

Mesostructured Pt/TiO_2 nanocomposites have been synthesized at different Pt (0–2 wt%) and anatase/rutile ratios through simple one-step sol–gel reactions. The as-made mesostructured hybrids were subjected to H_2 gas for 2 h at 450 °C to obtain ordered hexagonal mesoporous Pt/TiO_2 nanocomposites with highly crystalline TiO_2. Subsequently, the samples were calcined at 350 °C in air for 4 h to remove the surfactant. XRD data clearly show that biphasial anatase and rutile mixtures are formed by the addition of the Pt islands. The TEM results indicated that TiO_2 and Pt, are partly in close contact; the lattice fringes exhibit the typical distances, *i.e.*, Pt (111) (2.2 Å) and TiO_2 (101) (3.54 Å). TiO_2 nanoparticles with an average diameter of about 10 nm particles are not agglomerated and quite uniform in size and shape. Also, Pt nanoparticles are well dispersed and exhibit diameters of about 5–12 nm based on the Pt content. Our photocatalysts have been compared with colloidal 0.5 wt% Pt loaded onto commercial photocatalysts either UV-100 Hombikat or Aeroxide TiO_2 P25 by the determination of the initial rate of HCHO formation generated by the photooxidation of CH_3OH in aqueous suspensions to calculate the corresponding photonic efficiencies. The overall photocatalytic activities of 0.5 wt% Pt/TiO_2 nanocomposites are significantly 3-times higher than that of colloidal 0.5 wt% Pt loaded onto commercial photocatalysts either UV-100 Hombikat or Aeroxide TiO_2 P25. To the best of our knowledge, the measured photonic efficiency $\xi = 15.5\%$ of hexagonal mesostructured Pt/TiO_2 nanocomposites is found to be among the highest ξ values reported up to now. The superiority of Pt/TiO_2 is attributed to the bicrystalline (anatase/rutile) framework, large surface area, high crystallinity and mesoporous structure of Pt/TiO_2 nanocomposites.

Introduction

Mesoporous materials prepared through an assembly between organic surfactant molecules and inorganic species have seen a tremendous development since their discovery in the early 1990s.[1] Their tunable mesoporous structures, tailored framework composition, narrow pore size distribution, large surface area and large pore volume have stimulated active research works in different fields of application.[2] Mesoporous channels offer larger surface area and enhanced accessibility. Such a unique combination provides a new platform for design and fabrication of novel photoactive materials and devices, such as high-efficiency photocatalyst and photovoltaic.[3] Among those, photoactive mesoporous TiO_2 has attracted much attention because of its high surface-to-volume ratio, which is of great importance in photocatalysis, photosplitting water, and solar energy conversion.[4] Design of TiO_2 with well-defined mesoporous structure is a promising way to achieve high photocatalytic activity, since the ordered mesopore channels facilitate fast intraparticle molecular transfer,[5–7] while the large surface area may enhance the light harvesting and the adsorption for reactant molecules. Meanwhile, a high crystallization degree of photocatalysts is favorable for rapid transfer of photocharges from bulk to surface, which could inhibit the recombination between photoelectrons and holes, leading to enhanced quantum efficiency.[8,9] However, preparation of semiconductor oxides with both the ordered mesoporous structure and highly crystalline pore wall is usually a challenging task.[10,11] Since the anatase phase has a far higher photocatalytic activity than amorphous and rutile TiO_2, it is still a challenge to synthesize mesoporous TiO_2 containing the high crystallization of anatase phase and large surface area.[12–14] To the best of our knowledge, there are few reports on the synthesis of TiO_2 nanoparticles with stable anatase mesostructures,[3,14] which has an advantage in relatition

*[a]Advanced Materials Department, Central Metallurgical R&D Institute, CMRDI, P.O. Box 87, Helwan 11421, Cairo, Egypt.
E-mail: aismail@cmrdi.sci.eg, adelali11@yahoo.com*
[b]Leibniz Universität Hannover, Institut für Technische Chemie, Photocatalysis and Nanotechnology, Callinstrasse 3, 30167 Hannover, Germany

to photocatalytic and photoelectrochemical properties. For instance, mesoporous TiO_2 photocatalysts were proven to be much more active than nonporous TiO_2.[15,16] However, the integrity of the porous architecture is difficult to maintain if a catalyst is subsequently doped with heteroatoms at elevated temperatures. The porous framework often collapses when a catalyst is sintered at high temperatures.[15,16] Moreover, TiO_2 is usually used as a photocatalyst in two crystal structures: rutile and anatase. Anatase generally has much higher activity than rutile.[17] More interesting is the fact that the activity of P-25 (Degussa), which consists of anatase and rutile (4/1 w/w), exceeds that of pure anatase in several reaction systems.[18] Indeed, P-25 has frequently been used as a benchmark for photocatalysts. However, TiO_2 nanocrystals with an optimum either bicrystalline anatase/brookite or brookite/rutile ratio exhibited much higher photocatalytic activity than Degussa TiO_2 P25.[19]

The dispersion of noble metals on semiconductor particles are known to improve the photocatalytic electron transfer processes at the semiconductor interface.[15,20] It is, thus, reasonable to expect that electrons accumulated in a large extent within the metal nanoparticles thus improving the efficiency of electron-hole separation.[21] In the presence of O_2 (*i.e.* an efficient acceptor) noble metals can release the accumulated electrons thus leading to the formation of $\cdot O_2^-$ which can finally lead to $\cdot OH$. On the other hand, photoinduced holes (h^+) in TiO_2 can be scavenged by OH^- to generate $\cdot OH$.[22,23] Therefore, noble metals can play a twofold role: (i) reduce the e^-/h^+ recombination as a consequence of the electron transfer from TiO_2 to noble metals and (ii) enhance the photoreduction efficiency owing to the Fermi level equilibration, thus ultimately leading to a higher yield of $\cdot OH$.

As a photocatalytic test reaction, the photooxidation of CH_3OH to $HCHO$ by $\cdot OH$ attack is well established and investigated for powdered TiO_2,[24] TiO_2 (Evonik-Degussa) P25, Sachtleben Hombikat UV 100 and colloidal TiO_2[25] as well 20% TiO_2/SiO_2 and $TiO_2/SBA-15$[26] The efficiency of this photooxidation reaction very much depends on the photonic efficiency for the generation of $\cdot OH$ radicals. This primary step of HCHO formation initiates a series of degradation reactions that ultimately lead to mineralization of the pollutants. It has been reported that a considerable fraction of the $HCOOH$ formed on the photocatalyst surface is decomposed into CO_2 and H_2O on the spot without being released from the surface.[27,28] Thus, an experimental method for the detection of the quantity of photons absorbed by aqueous TiO_2 dispersions was developed.[29] Among the pure TiO_2 phases P25 (Evonik-Degussa) was found to exhibit the highest activity but by using $Fe_2O_3–TiO_2$,[30] $Pt@TiO_2$[31] and mesoporous noble metals/TiO_2 nanocomposites for the same reaction,[15] the photonic efficiencies could be enhanced by a factor of two. The photocatalytic activity of TiO_2 depends on various parameters, including crystallinity, impurities, surface area, and density of surface hydroxy groups; however, the most significant factor is its crystal form.[18]

In this contribution, we report one-step synthesis of hexagonal *P6m* mesoporous Pt/TiO_2 nanocomposites at different Pt content (0–2 wt%) and anatase/rutile ratios. Our prepared photocatalysts have been compared with colloidal Pt loaded onto the commercial photocatalysts Aeroxide TiO_2 P25 (Evonik AG) and Sachtleben Hombikat UV-100 by the determination of the initial rate of HCHO formation generated by the photooxidation of CH_3OH in aqueous suspensions to calculate the corresponding photonic efficiencies. The overall photocatalytic activities of 0.5 wt% Pt/TiO_2 composites are significantly 3-times higher than that of colloidal 0.5 wt% Pt loaded onto commercial photocatalysts either Hombikat UV-100 or Aeroxide TiO_2 P25.

2.   Experimental

Materials. The block copolymer surfactant EO_{106}–$PO_{70}EO_{106}$(F-127,EO = $–CH_2CH_2O–$, PO = $–CH_2(CH_3)CHO–$), MW 12 600 g mol^{-1}), $Ti(OC(CH_3)_3)_4$ (TBOT), HCl, CH_3OH, C_2H_5OH, CH_3COOH and chloroplatinic acid (H_2PtCl_6) were purchased from Sigma-Aldrich. Commercial TiO_2 (Hombikat UV-100) and Aeroxide TiO_2 P25 (Evonik AG) were kindly provided by Evonik-Degussa and Sachtleben Chemie GmbH respectively.

Preparation of Pt/TiO_2 nanocomposites. Mesoporous Pt/TiO_2 nanocrystals were synthesized through a simple one-step sol–gel process in the presence of the F127 triblock copolymer as structure directing agent. In a typical procedure, to minimize possible variables, the molar ratio of each reagent in the starting solution was fixed at $TiO_2/F127/C_2H_5OH/HCl/CH_3COOH$ = 1 : 0.02 : 50 : 2.25 : 3.75 molar ratios. In particular, 1.6 g of F127, 2.3 mL of CH_3COOH and 0.74 mL of HCl were dissolved in 30 ml of ethanol and then added to 3.5 ml of TBOT.[32] The calculated amount of H_2PtCl_6 was added to the F127–TBOT–CH_3COOH mesophase to obtain 0.1, 0.3, 0.5, 1 and 2 wt% Pt/TiO_2 composites and the mixture was stirred vigorously for 60 min and transferred into a Petri dish. Ethanol was subsequently evaporated at 40 °C and a relative humidity of 40% for 12 h followed by the transfer of the sample into a 65 °C oven and aging for an additional 24 h. The as-made mesostructured hybrid PtO/TiO_2 materials were subjected to H_2 gas for 2 h at 450 °C to obtain highly ordered hexagonal *P6m* mesoporous Pt/TiO_2 and highly crystalline TiO_2. Subsequently, the Pt/TiO_2 materials calcined at 350 °C in air for 4 h at a heating rate of 1 °C min^{-1} and a cooling rate of 2 °C min^{-1} to remove the surfactant.

Preparation of 0.5 wt% colloidal Pt/Hombikat UV-100 or Aeroxide P-25. Colloidal Pt (particle diameters *ca.* 3 nm) were prepared by reduction of H_2PtCl_6 with sodium citrate.[33] Excess ions in the resulting colloidal suspension were removed with an ion exchange resin (Amberlite MBl) until a specific conductivity of *ca.* 3 μS cm^{-1} was reached. Pt loaded TiO_2 was prepared by suspending 0.25 g of either Aeroxide TiO_2 P25 (Evonik AG) and Hombikat UV-100 powder in 80 mL of deionized water by sonication, followed by the addition of the desired amount of as-prepared colloidal Pt under continuous magnetic stirring. The stirring was kept overnight to ensure the homogeneous dispersion of the Pt nanoparticles. After evaporation under vacuum at room temperature, a greyish powder was obtained. The obtained powder was dried at 60 °C in an oven overnight.

Characterization

Transmission electron microscopy (TEM) was conducted at 200 kV with a JEOL JEM-2100F-UHR field-emission instrument equipped with a Gatan GIF 2001 energy filter and a 1k-CCD camera in order to obtain EEL spectra. Wide angle X-ray diffraction (WXRD) data were acquired on a Bruker AXS D4 Endeavour X diffractometer using Cu-K$\alpha_{1/2}$, $\lambda\alpha_1 = 154.060$ pm, $\lambda\alpha_2 = 154.439$ pm radiation and small angle X-ray diffraction (SXRD) patterns were recorded on a Bruker D8 advance. The nitrogen adsorption and desorption isotherms at 77 K were measured using a Quantachrome Autosorb 3B after the samples were vacuum-dried at 200 °C overnight. The sorption data were analyzed using the Barrett-Joyner-Halenda (BJH) model with Halsey equation.[34]

Photocatalytic activity tests

The quartz photoreactor was filled with 75 mL aqueous solution of methanol at a concentration 30 mM. UV irradiation was performed by a 450 W medium pressure xenon lamp (Osram) placed inside a quartz jacket and equipped with a cooling tube. The lamp was switched on 30 min prior to the start of the reaction to stabilize the power of its emission at $\lambda > 320$ nm (a cut-off filter was used to remove light with wavelengths below 320 nm) and the reactor was cooled by circulation of H_2O. The temperature of the cooling water was stabilized to perform the reactions at 25 °C. Photooxidation reactions were carried out suspending 0.5 g L^{-1} of the photocatalysts with oxygen being purged through the reaction vessel continuously. The suspensions were sonicated at the desired aqueous solution of methanol (30 mM) before the experiment was started and they were stirred in the dark for 30 min to reach the adsorption equilibrium prior to irradiation. HCHO samples were withdrawn at regular intervals from the upper part of the reactor with the catalyst being removed from the liquid phase by filtration through nylon syringe filters (pore size: 0.45 µm). The photooxidation rate was determined by measuring the HCHO generated as a result of methanol oxidation during the first 60 min of illumination employing the Nash method.[35] The detection limit for HCHO determined by the Nash method is 1.66 µM. The relative error of the measured HCHO concentration was ±5% as judged from repeated runs under identical conditions. This method is based on the reaction of formaldehyde with acetylacetone and ammonium acetate to form a yellow coloured product with a maximum of absorbance at 412 nm. Measurements were carried out using a Varian Cary 100 Scan UV-vis spectrophotometer, following an incubation time of 15 min at 60 °C. Photonic efficiency (ζ) is useful to compare process efficiencies using a given photocatalyst material and a given standard test molecule. The photonic efficiency was calculated for each experiment as the ratio of the HCHO formation rate and the incident light intensity as given in the following equation[36]

$$\xi = \frac{r \times 100}{I}$$

where ξ is the photonic efficiency (%), r the photooxidation rate of methanol (mol $L^{-1}s^{-1}$), and I the incident photon flux (4.94 ×

10^{-6} Ein $L^{-1}s^{-1}$). The UV-A incident photon flow was determined by ferrioxalate actinometry.[37]

Results and discussion

Mesoporous Pt/TiO$_2$ nanocrystals have been synthesized through a simple one-step sol–gel process in the presence of the F127 triblock copolymer as the structure directing agent. It confirms that complexation of metal precursor with the functional segment of the block copolymer is essential to accomplish smaller particle size, its narrow distribution and phase specific dispersion.[38] To homogenously distribute platinum nanoparticles into the titania framework, we utilized a multicomponent assembly approach, where surfactant, titania, and PtO were assembled in an one-step process. The as-made mesostructured hybrids PtO/TiO$_2$ materials were subjected to H$_2$ gas for 2 h at 450 °C to obtain hexagonal *P6m* mesoporous Pt/TiO$_2$ and highly crystalline TiO$_2$. Subsequently, Pt/TiO$_2$ samples were calcined at 350 °C in air for 4 h to remove the surfactant.[15a,32] The small angle X-ray scattering (SAXS) patterns of highly ordered mesoporous Pt/TiO$_2$ as-made and of Pt/TiO$_2$ nanocomposites at different Pt contents calcined at 450 °C are shown in Fig. 1. The as-made sample shows two well-resolved peaks, which can be indexed to the (10) and (20) Bragg reflections confirming an ordered 2D-hexagonal mesostructure of the *P6m* space group.[32] After calcination at 450 °C, the observed intensities and the broadness of the peaks prove that a long-range order declines in the undoped TiO$_2$ and Pt/TiO$_2$ nanocomposite at low Pt (0, 0.1, 0.3, and 0.5 wt%) contents. With increasing Pt content (1 and 2 Pt wt%) the diffraction peaks are becoming weaker with the (10) and (20) reflections indicating that the long-range ordering of the mesopores is already disappearing. It is evident that after the collapses of the hexagonal ordering even the pore channels themselves start to collapse and disordered mesostructures of crystalline TiO$_2$ are obtained. After template removal, the structural regularity declines but the lattice parameters calculated from the d_{10} value decrease only from 12.96 to 11.22 nm indicating an approx. 13.42% contraction of the structure. Fig. 2 shows the WAXRD patterns of the mesoporous Pt/TiO$_2$ nanocomposites
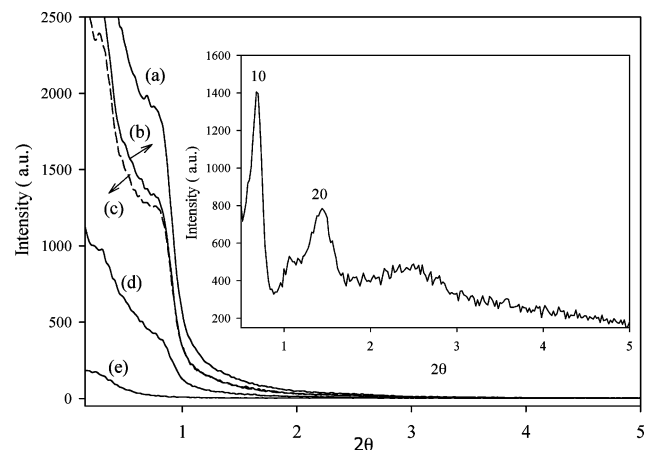

Fig. 1 SAXS patterns of as made Pt/TiO$_2$ (inset) and mesoporous Pt/TiO$_2$ nanocomposites calcined at 450 °C at different Pt wt% 0 (a), 0.3 (b), 0.5 (c), 1 (d) and 2 (e).

Table 1 Textural properties of nanocomposites Pt/TiO$_2$ calcined at 450 °C and Pt colloidal on either commercial Hombikat UV100 or Degussa P-25 and their photocatalytic properties

Photo-catalysts	S$_{BET}$/m^{2}g^{-1}	Cs$_{TiO_2}$ (nm)	[a]Phase content form (%) Anatase	Rutile	r × 10^7 (mol L^{-1}s^{-1})	ξ (%)	d$_{100}$ (nm)	Unit cell size/nm	Pore wall/nm	Vp (cm^3 g^{-1})	Dp (nm)
TiO$_2$ (As-made)	—	—	—	—	—	—	12.96	14.98	—	—	—
Undoped TiO$_2$	176	13.5	100.0	—	3.93	7.9	11.39	13.16	6.66	0.3	6.5
0.1 wt% Pt/TiO$_2$	169	11.6	77.5	22.5	4.76	9.6	11.24	12.98	6.68	0.29	6.3
0.3 wt% Pt/TiO$_2$	162	11.6	74.1	25.7	6.66	13.4	11.22	12.96	6.86	0.29	6.1
0.5 wt% Pt/TiO$_2$	155	11.5	65.5	34.0	7.66	15.5	11.38	13.15	7.15	0.24	6.0
1 wt% Pt/TiO$_2$	144	11.7	74.3	24.7	5.74	11.6	11.15	12.87	6.77	0.23	6.1
2 wt% Pt/TiO$_2$	134	11.7	80.1	17.7	4.42	8.9	11.16	12.90	6.20	0.21	6.7
0.5 wt% Pt/P-25	45	25.0	80.0	20.0	2.01	4.1	—	—	—	—	—
0.5 wt% Pt/UV-100	225	10.0	100.0	—	2.78	5.6	—	—	—	0.29	3.35

[a] Rietveld analysis, S$_{BET}$ surface area, C$_{S\,TiO_2}$ crystallite size of TiO$_2$, r HCHO formation rate, ξ Photonic efficiency, Vp pore volume, Dp pore diameter.

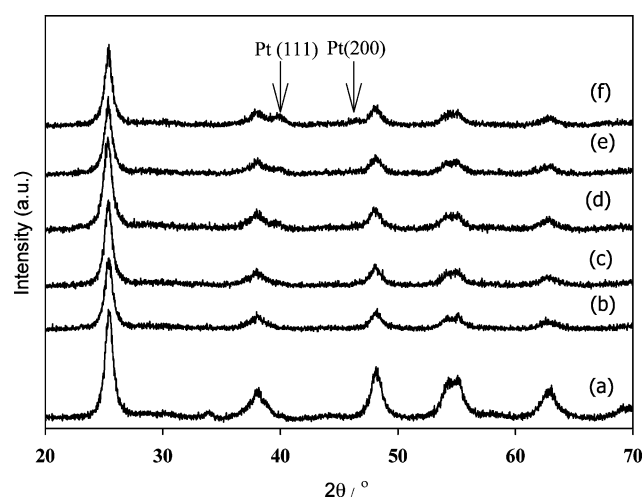**Fig. 2** WXRD of mesoporous Pt/TiO$_2$ nanocomposites calcined at 450 °C at different Pt wt% 0 (a), 0.1 (b), 0.3 (c), 0.5 (d), 1 (e) and 2 (f). Shifted for sake of clarity.

Fig. 3 N$_2$ sorption isotherms and pore size distributions (inset) of the mesoporous of Pt/TiO$_2$ nanocomposites calcined at 450 °C at different 0.5, 1 and 2 wt% Pt.

at different Pt contents. Clearly, all the diffraction patterns can be indexed to the anatase phase, respectively. With increasing Pt content, the peaks assigned to the anatase phase decrease and slightly rutile phase is formed. The quantitative phase composition and crystallite diameter of undoped TiO$_2$ and Pt/TiO$_2$ nanocomposites at different Pt content and as evident from the Rietveld analysis of the XRD data are given in Table 1. XRD data clearly show that biphasial anatase and rutile mixtures are formed by the addition of Pt nanoparticles even at small concentration. These results indicate that there is a phase transformation from anatase to rutile nanoparticles with Pt addition (Table 1). At 0.1 and 0.3 wt% Pt/TiO$_2$, no crystalline phase involving Pt can be observed, suggesting that either the Pt is highly dispersed in the TiO$_2$ network or that the Pt content is below the detection limit. On the other hand, at 0.5, 1 and 2 wt% Pt/TiO$_2$, XRD patterns exhibit diffractions at around $2\theta = 39.8°$ and 46.3°, which can be indexed as (111) and (200) reflections of the crystalline Pt (JCPDF 01-1194) possessing a face-centered cubic structure with an Fm3m space group.[39] These peaks are weak and broad, indicating the nanocrystalline nature of the platinum particles encapsulated into TiO$_2$ network.

Fig. 3 shows nitrogen adsorption–desorption isotherms and Barrett–Joyner–Halenda (BJH) pore-size distribution plots of
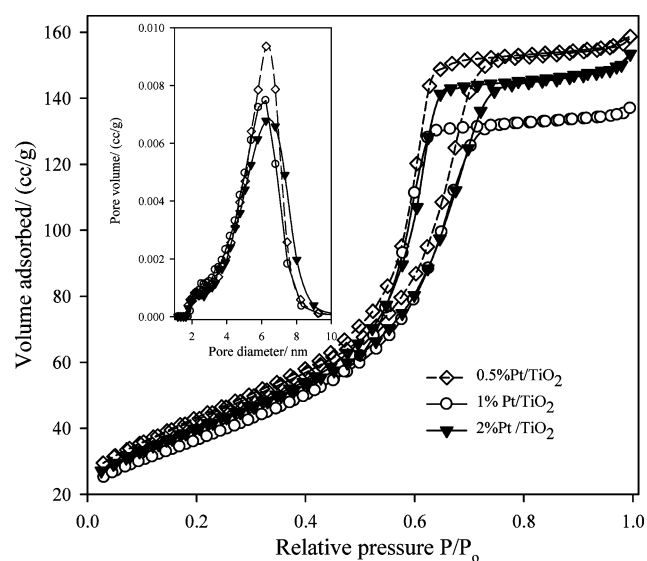
the mesoporous Pt/TiO$_2$ nanocomposites at different Pt contents. The samples show similar type-IV isotherms, which are representative of mesoporous solids.[34] The sharpness of the inflection resulting from capillary condensation at relative pressures p/p_0 between 0.45 and 0.8 is characteristic for mesopores in two-dimensional hexagonal symmetry. The mesoporous TiO$_2$ has high surface areas of 174 m^{2}g^{-1} and large pore volumes of 0.3 cm^{3}g^{-1}; they are gradually reduced to 134 m^{2}g^{-1} and 0.21 cm^{3}g^{-1}, respectively, as a result of the Pt addition (Table 1). The slight decrease in pore size with the Pt addition at low content reveals that the thickness of the pore walls increases concomitantly from 6.6 to 7.15 nm. Then the pore sizes were decreased at high Pt content 1 and 2 wt% Pt to 6.77 and 6.20 nm respectively, as a result of the Pt nanoparticles blocking the mesopores and collapsing mesostructure of Pt/TiO$_2$ nanocomposites. Compared with the size of the TiO$_2$ nanocrystallites between 10 ± 2 nm (Table 1), the wall thickness is found to be slightly smaller, implying that some of the TiO$_2$ nanocrystals could partially pierce even into the channel space,[40] which is particularly evident from the HRTEM images (Fig. 4e &f).
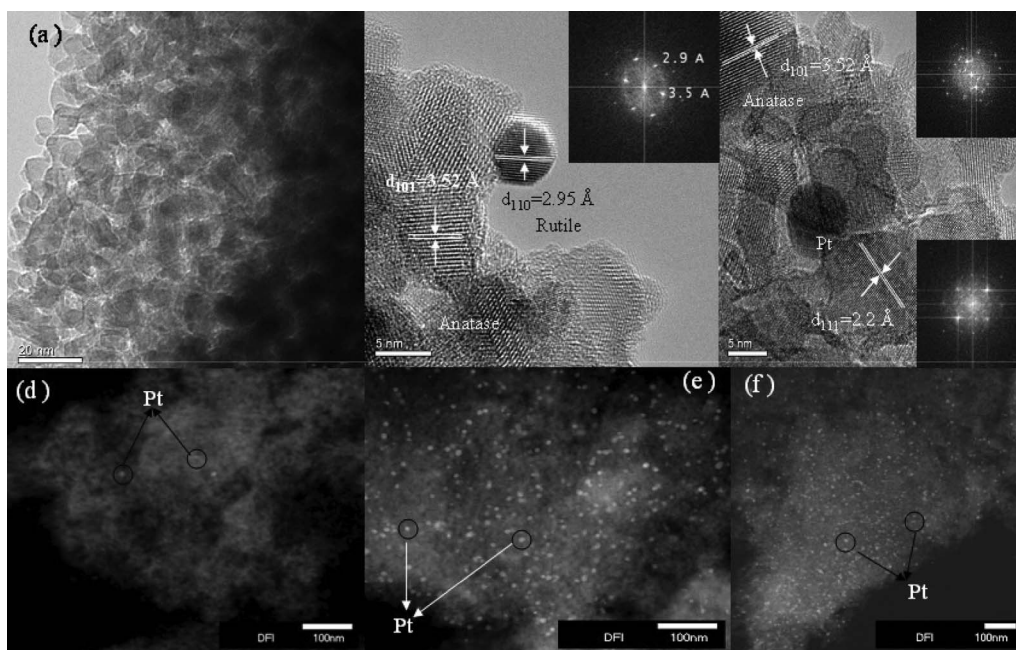
Fig. 4 TEM images of mesoporous 0.5 wt% Pt/TiO_2 nanocomposites calcined at 450 °C for 4 h (a), HRTEM image at 0.5 wt% Pt/TiO_2 (b) and 2 wt% Pt/TiO_2 nanocomposites (c). Dark-field TEM image of mesoporous 0.5 wt% Pt/TiO_2 (d) and 1 wt% Pt/TiO_2 (e), 2 wt% Pt/TiO_2 (f).

Fig. 4 TEM images of mesoporous 0.5 wt% Pt/TiO_2 nanocomposites calcined at 450 °C for 4 h (a) demonstrates that TiO_2 nanoparticles with an average diameter of about 10 nm particles are not agglomerated and quite uniform in size and shape. The high-resolution TEM micrograph in Fig. 4b shows the rutile and anatase lattice. The corresponding Fourier transform (Fig. 4b, inset) confirms the orientation of the anatase and rutile nanoparticles. Hence, the anatase and rutile particles exhibit primarily (101) and (110)-type facets respectively (Fig. 4b). As seen in the HRTEM images (Fig. 4c) the atomic planes of the Pt particles are separated by 2.2 Å, which agrees with the (111) lattice spacing of face-centered cubic Pt. TiO_2 and Pt, are partly in close contact as seen most impressively in Fig. 4c; the lattice fringes exhibit the typical distances, *i.e.*, Pt (111) (2.2 Å) and TiO_2 (101) (3.54 Å). Furthermore, dark-field TEM image of mesoporous Pt/TiO_2 nanocomposites are shown in Fig. 4d,e&f for 0.5 Pt, 1 Pt and 2 Pt wt% respectively. TEM images (Fig. 4d,e&f) of mesoporous Pt/TiO_2 clearly show Pt nanoparticles are well dispersed and exhibit diameters of about 5–15 nm based on the Pt nanoparticles addition. Although being that large there are no indications that the Pt nanoparticles are not located on the outer surface of the mesoporous TiO_2 network. In such case, an increased concentration at the rims of the particles should be observable on the TEM pictures – this is, however, not the case. Instead the growing Pt particles seem to create new pores in the TiO_2 network through destruction of parts of the channel walls. Such creation of new pores is well known *e.g.* from the growth of Pt particles in zeolites.[41]

Photocatalytic activity

The photocatalytic activities of all newly synthesized photocatalysts were evaluated for the photooxidation of CH_3OH to HCHO. On the TiO_2 surface the photogenerated holes react with

OH^- ions or H_2O molecules, yielding highly oxidative hydroxyl ($^\bullet OH$) radicals, which are the key oxidants in the photocatalytic oxidation process.[22] These radicals quickly react with absorbed CH_3OH, which is further oxidized to HCHO and finally to CO_2. The photogenerated electrons are consumed by adsorbed oxygen molecules to form $O_2^{\bullet-}$ and/or H_2O_2, which also contribute to the oxidation of CH_3OH *via* the intermediate formation of $^\bullet OH$ radicals. Obviously, the production of HCHO should be proportional to that of the hydroxyl radical, $^\bullet OH$, which plays a vital role in photocatalysis. Therefore, the photonic efficiency of HCHO can be used as an indicator of $^\bullet OH$ production, and hence can be used to compare different photocatalysts.[24] Considering the reaction dynamics during the entire photocatalytic process, the photocatalytic efficiency will be determined by the number of photogenerated charge carriers which can avoid the recombination reaction. The photonic efficiency (ζ) was calculated for each experiment as the ratio of the HCHO formation rate from photocatalytic oxidation of CH_3OH and the incident light intensity. Fig. 5 shows the change of the HCHO concentration as a function of the irradiation time for the mesoporous Pt/TiO_2 nanocomposites at different Pt contents. A linear relation of the HCHO concentration with irradiation time was obtained during the first 60 min of illumination. From this figure the HCHO formation rate was found to increase from $3.93 \times 10^{-7} - 7.66 \times 10^{-7}$ mol $L^{-1}s^{-1}$ with increasing Pt content from 0–0.5 wt% and then decrease to 4.42×10^{-7} mol $L^{-1}s^{-1}$ at 2 wt% Pt whereas the HCHO formation rate using colloidal 0.5 wt% Pt loaded onto Aeroxide TiO_2 P25 and Hombikat UV-100 are 2.01×10^{-7} and $2.78 10^{-7}$ mol $L^{-1}s^{-1}$ respectively. Fig. 6 shows the photonic efficiencies of CH_3OH photooxidation for Pt/TiO_2 nanocomposites and Pt colloidal loaded onto Aeroxide TiO_2 P25 and Hombikat UV-100. The data obtained during the illumination of the Pt/TiO_2 nanocomposites with UV light are shown in Fig. 6 and summarized in Table 1. They
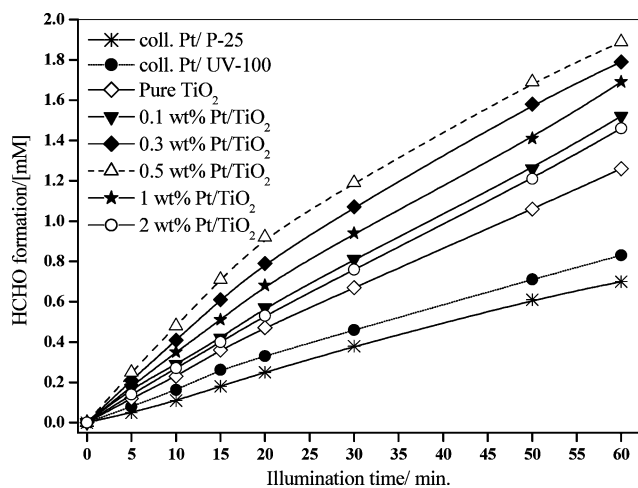
Fig. 5 HCHO formation as a function of illumination time over mesoporous Pt/TiO$_2$ nanocomposites at different Pt content 0, 0.1, 0.3, 0.5, 1 and 2 wt% and colloidal Pt loaded onto the commercial photocatalysts Aeroxide TiO$_2$ P25 (Evonik AG) and Hombikat UV-100. Photocatalyst loading, 0.5 g l^{-1}; 30 mM aqueous CH$_3$OH (O$_2^-$ saturated, natural pH; T = 20 °C); reaction volume, 75 ml; I$_o$ = 4.49 × 10^{-6} Einstein L^{-1} s^{-1} (*ca.* >320 nm).
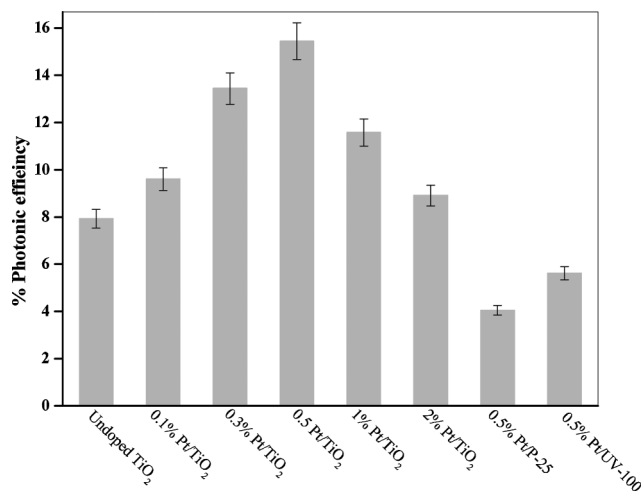

Fig. 6 Photooxidation of methanol to produce HCHO over mesoporous Pt/TiO$_2$ nanocomposites at different Pt content 0, 0.1, 0.3, 0.5, 1 and 2 wt%. and colloidal Pt loaded onto the commercial photocatalysts Aeroxide TiO$_2$ P25 (Evonik AG) and Hombikat UV-100. Photocatalyst loading, 0.5 g l^{-1}; 30 mM aqueous CH$_3$OH (O$_2^-$ saturated, natural pH; T = 20 °C); reaction volume, 75 ml; I$_o$ = 4.49 × 10^{-6} Einstein L^{-1} s^{-1} (*ca.* >320 nm).

reveal that the photonic efficiency increases with increasing Pt content up to 0.5 wt% Pt/TiO$_2$ with the maximum photonic efficiency being 15.5%. Subsequently, the photonic efficiency gradually decreases with increasing Pt/Ti ratio reaching a value of 8.9% for the sample containing 2 wt% Pt. It is clearly seen that the mesoporous Pt/TiO$_2$ nanocomposites are more photoactive than the commercially available photocatalysts either UV-100 or Aeroxide TiO$_2$ P25 (Table 1 and Fig. 6). In the presence of undoped mesoporous TiO$_2$ nanoparticles the photonic efficiency of HCHO formation, ζ HCHO, is *ca.* 7.9% (Table 1). The photocatalytic activities of undoped

mesoporous TiO$_2$ nanoparticles exceed that of either colloidal Pt loaded commercial Hombikat UV-100 or P-25, although the Hombikat TiO$_2$ was calcined at 450 °C, and is, thus, much more crystalline (100% anatase) and surface area than most of newly prepared Pt/TiO$_2$ nanocomposites. This difference cannot be explained by different surface areas, because this is even higher for the Hombikat material (Table 1). Such high photonic efficiencies of the mesoporous Pt/TiO$_2$ as compared with either colloidal Pt loaded onto commercial Hombikat UV-100 or Aeroxide TiO$_2$ P25 can be attributed to several effects, such as a lower light scattering effect of the ordered mesopores, an accumulated local concentration of ·OH,[42] or a fast transport of the target molecule CH$_3$OH to the active sites due to the facile diffusion of the CH$_3$OH through the ordered porous network, which for the Hombikat UV-100 and Aeroxide TiO$_2$ P25 samples are hindered by the heterogeneities existing in the bulk sample.

As shown in Fig. 6 and Table 1, 0.5 wt% Pt/TiO$_2$ which consists of 65% anatase and 35% rutile (according to the Rietveld phase analysis) exhibit a higher photocatalytic activity than 0.5 wt% colloidal Pt loaded onto commercial photocatalysts UV-100 and Aeroxide P25. This can be explained by the band gaps Eg of anatase (a) and rutile (b) are 3.2 and 3.0 eV respectively.[43] The fact that the conduction band (CB) edge of TiO$_2$ anatase is about 0.2 eV (the difference in Eg between anatase and rutile is almost equal to that in the CB edge) higher than that of TiO$_2$ rutile is thought to facilitate interfacial electron transfer, and the energy barrier would suppress back electron transfer. Consequently, the holes left in the valence band of TiO$_2$ anatase efficiently oxidize CH$_3$OH, while the electrons moving into TiO$_2$ rutile are consumed by the reduction of O$_2$.[44] The difference in activity found for undoped mesoporous TiO$_2$ and doped ones thus suggests that the rate of electron transfer from mesoporous TiO$_2$ nanocrystals to adsorbed oxygen is increased when Pt is incorporated into mesoporous TiO$_2$. This will lead to better charge carrier separation and thus to an increase of the photocatalytic activity. Moreover, by comparing the reaction rate per unit anatase, we can find that too much anatase will retard the photodegradation process, indicating that the proper amount of rutile is of certain benefit. Such a synergetic effect, also referred to as 'mixed phase effect', is supposed to efficiently prohibit the recombination of photogenerated electron-hole pairs by transferring the exited electrons from one phase to another.[8] Therefore, both the regular open pore morphology and the biphase structure are playing crucial roles in determining the sample's photoactivity. A recent result demonstrated that rapid electron transfer, occurring from rutile conduction band to lower energy anatase lattice trapping sites in mixed-phase titania P25, leads to a more stable charge separation. The electron-transfer process causes the existence of catalytic hot spots at anatase/rutile interface.[45] However, this process is critically dependent on the small particle size of rutile phase and intimate contact between two phases.[45] The small size of rutile and intimate contact with anatase facilitate the electron transfer at the interface. In our case, rutile phase obtained was formed at 450 °C instead of calcination at high temperature. The crystal size of <5 nm (Fig. 4b) of the rutile phase is relatively small and comparable to that of the crystal size anatase phase 10 nm (Table 1).

A second explanation for the higher photocatalytic activity of the mesoporous 0.5 wt% Pt/TiO_2 nanocomposites in comparison Pt/TiO_2 nanocomposites at high Pt content (1 and 2 wt%) might be the size of the Pt particles. Our results indicated that mesoporous TiO_2 is likely to exhibit better photocatalytic CH_3OH oxidation than Pt colloidal loaded onto either UV-100 or P25. But, the photonic efficiency of mesoporous TiO_2 is lower than Pt/TiO_2 nanocomposites. This has been attributed to a rate control by rather slow reduction of molecular oxygen by the trapped photoelectrons, whereby e^-/h^+ recombination is favored.[25] The purpose of loading TiO_2 with Pt is to generate at the interface between Pt and TiO_2 a Schottky barrier, which effectively captures the photogenerated electrons and reduces the rate of electron-hole recombination.[46] The interface being maximum at low Pt nanoparticles content and high dispersion, too large Pt particles (more than 0.5 wt%) could also act as recombination centers, detrimental to photocatalysis by hindering or avoiding the active photogenerated charge transfer to the reactant species at the surface.[47] Therefore, the highest activity observed for the 0.5 wt% Pt/TiO_2 nanocomposites can be ascribed to the most efficient charge separation through the mesopore charge transfer.[48] Although, the average particle sizes of colloidal Pt loaded onto UV-100 and TiO_2 P25 are 3 nm and highly dispersed and their sizes is smaller than Pt particles (5 nm) in 0.5 wt% Pt/TiO_2 nanocomposites, the photonic efficiencies of Pt loaded onto the commercial photocatalysts Aeroxide TiO_2 P25 and UV-100 are smaller three-times than 0.5 wt% Pt/TiO_2 nanocomposites. These results additionally confirm the importance of mesostructure of the photocatalysts and it is a promising way to achieve high photocatalytic activity since the ordered mesopore channels facilitate fast intraparticle molecular transfer.[5–7]

It was observed that in this three-dimensional solid/surface state framework the excited TiO_2 nanoparticle can transfer the absorbed energy through the mesoporous hexagonal TiO_2 network to other ground-state TiO_2. Through the so-called antenna mechanism[49] the resulting energetic coupling throughout a three-dimensional TiO_2 network will enable an energy and/or exciton transfer from the particle where the initial photon absorption took place to the particle where the electron transfer process finally occurs. Consequently, the probability of electron transfer to the Pt particle is increased by an increased CH_3OH diffusion through the pores of the nanostructures. Once the energy has reached the particle with the adsorbed methanol, the latter will act as a hole trap thus inducing the separation of the original exciton. Thus, the mesoporous TiO_2 networks will act as an antenna system transferring the photon energy from the location of light absorption to the location of reaction. Within this antenna model, it can be imagined that the overlap of the energy bands of the TiO_2 nanoparticles forming this network will result in unified energy bands for the entire system enabling a quasi-free movement of the photogenerated charge carriers throughout.[15,30,48a]

Assuming a Schottky contact between the mesoporous titanium dioxide network and the noble metal particle, the Pt particles then serve as active sites for the reduction of molecular oxygen, on which the trapped photogenerated electrons are transferred to oxygen producing O_2^- radicals. It should be noted that it is frequently overseen that this latter process is really the 'bottle-neck' in most photocatalytic transformations being the rate-determining step due to its very small thermodynamic driving force. Thus its acceleration through the electron transfer catalysis induced by the Pt deposits will result in the observed increase in the yield of the photocatalytic methanol oxidation.

Conclusions

Mesostructured Pt/TiO_2 nanocomposites at different Pt (0–2 wt%) and anatase/rutile ratios through simple one-step sol–gel reactions have been achieved. The overall photocatalytic activities of 0.5 wt% Pt/TiO_2 nanocomposites are significantly 3-times higher than that of colloidal 0.5 wt% Pt loaded onto commercial photocatalysts either UV-100 Hombikat or Aeroxide TiO_2 P25. The superiority of Pt/TiO_2 in our case is attributed to the bicrystalline framework, large surface area, high crystallinity and mesoporous structure of Pt/TiO_2 nanocomposites. With these characteristics of newly prepared photocatalysts, the separation of photoinduced electron hole pairs is favorable. After all, the separation of the electron hole pairs is responsible for photocatalytic activity. The regular open pore morphology and the biphase structure are playing crucial roles in promoting the diffusion of reactants and products, enhancing the photocatalytic activity by facilitating access to the reactive sites on the surface of photocatalyst.

Acknowledgements

References

1 C. T. Kresge, M. E. Leonowicz, W. J. Roth, J. C. Vartuli and J. S. Beck, *Nature*, 1992, **359**, 710.
2 (*a*) S. Rodrigues, S. Uma, I. N. Martyanov and K. Klabunde, *J. Catal.*, 2005, **233**, 405; (*b*) A. M. Liu, K. Hidajat, S. Kawi and D. Y. Zhao, *Chem. Commun.*, 2000, 1145; (*c*) G. Palmisano, V. Augugliaro, M. Pagliaro and L. Palmisano, *Chem. Commun.*, 2007, 3425.
3 J. C. Yu, X. C. Wang and W. Ho, *Adv. Funct. Mater.*, 2004, **14**, 1178.
4 D. M. Antonelli and J. Y. Ying, *Angew. Chem., Int. Ed. Engl.*, 1995, **34**, 2014.
5 H. X. Li, Z. F. Bian, J. Zhu, Y. N. Huo, H. Li and Y. F. Lu, *J. Am. Chem. Soc.*, 2007, **129**, 4538.
6 J. C. Yu, G. S. Li, X. C. Wang, X. L. Hu, C. W. Leung and Z. D. Zhang, *Chem. Commun.*, 2006, 2717.
7 (*a*) A. A. Ismail and D. W. Bahnemann, *ChemSusChem*, 2010, **3**, 1057–1062; (*b*) A. A. Ismail, T. A. Kandiel and D. W. Bahnemann, *J. Photochem. Photobiol., A*, 2010, **216**, 183–193.
8 D. Sukkim and S.-Y. Kwak, *Environ. Sci. Technol.*, 2009, **43**, 148–151.
9 A. Fujishima, T. N. Rao and D. A. Tryk, *J. Photochem. Photobiol., C*, 2000, **1**, 1.
10 P. D. Yang, D. Y. Zhao, D. I. Margolese, B. F. Chmelka and G. D. Stucky, *Nature*, 1998, **396**, 152.
11 M. H. Bartl, S. P. Puls, J. Tang, H. C. Lichtenegger and G. D. Stucky, *Angew. Chem., Int. Ed.*, 2004, **43**, 3037.
12 L. M. Huang and Q. Z. Li, *Chem. Lett.*, 1999, **28**, 829.
13 J. M. Yu, L. Z. Zhang, Z. Zheng and J. C. Zhao, *Chem. Mater.*, 2003, **15**, 2280.
14 (*a*) L. Chen, B. Yao, Y. Cao and K. Fan, *J. Phys. Chem. C*, 2007, **111**, 11849–11853; (*b*) H. Shibata, T. Ogura, T. Mukai, T. Ohkubo, H. Sakai and M. Abe, *J. Am. Chem. Soc.*, 2005, **127**, 16396–16397; (*c*) Y. D. Wang, C. L. Ma, X. D. Sun and H. D. Li, *Mater. Lett.*, 2002,

54, 359; (*d*) T. Y. Peng, A. Hasegawa, J. R. Qiu and K. Hirao, *Chem. Mater.*, 2003, **15**, 2011.

15 (*a*) A. A. Ismail, D. W. Bahnemann, L. Robben, V. Yarovyi and M. Wark, *Chem. Mater.*, 2010, **22**, 108–116; (*b*) A. A. Ismail, D. W. Bahnemann, I. Bannat, M. Wark and M. Wark, *J. Phys. Chem. C*, 2009, **113**, 7429–7435; (*c*) A. A. Ismail and D. W. Bahnemann, *J. Adv. Oxid. Technol.*, 2009, **12**, 9–15.

16 (*a*) X. C. Wang, J. C. Yu, C. M. Ho, Y. D. Hou and X. Z. Fu, *Langmuir*, 2005, **21**, 2552; (*b*) J. C. Yu, X. C. Wang and X. Z. Fu, *Chem. Mater.*, 2004, **16**, 1523.

17 K. Tanaka, M. F. V. Capule and T. Hisanaga, *Chem. Phys. Lett.*, 1991, **29**, 73.

18 (*a*) H. Tada and M. Tanaka, *Langmuir*, 1997, **13**, 360; (*b*) Z. Ding, G. Q. Lu and P. F. Greenfield, *J. Phys. Chem. B*, 2000, **104**, 4815; (*c*) J. Jia, T. Ohno, Y. Masaki and M. Matsumura, *Chem. Lett.*, 1999, 963.

19 (*a*) H. Xu and L. Zhang, *J. Phys. Chem. C*, 2009, **113**, 1785–1790; (*b*) J. C. Yu, L. Zhang and J. Yu, *Chem. Mater.*, 2002, **14**, 4647–4653.

20 V. Subramanian, E. Wolf and P. V. Kamat, *J. Phys. Chem. B*, 2001, **105**, 11439–11446.

21 (*a*) P. D. Cozzoli, R. Comparelli, E. Fanizza, M. L. Curri, A. Agostiano and D. Laub, *J. Am. Chem. Soc.*, 2004, **126**, 3868–3879; (*b*) P. D. Cozzoli, M. L. Curri and A. Agostiano, *Chem. Commun.*, 2005, 3186–3188.

22 M. R. Hoffmann, S. T. Martin, W. Choi and D. W. Bahnemann, *Chem. Rev.*, 1995, **95**, 69–96.

23 H. Goto, Y. Hanada, T. Ohno and M. Matsumura, *J. Catal.*, 2004, **225**, 223–229.

24 L. Sun and J. R. Bolton, *J. Phys. Chem.*, 1996, **100**, 4127.

25 C. Y. Wang, J. Rabani, D. W. Bahnemann and J. K. Dohrmann, *J. Photochem. Photobiol., A*, 2002, **148**, 169–176.

26 (*a*) J. Marugan, D. Hufschmidt, M.-J. Lopez-Munoz, V. Selzer and D. W. Bahnemann, *Appl. Catal., B*, 2006, **62**, 201; (*b*) J. M. Stokke and D. W. Mazyck, *Environ. Sci. Technol.*, 2008, **42**, 3808–3813.

27 O. Legirini, E. Oliveros and A. M. Braun, *Chem. Rev.*, 1993, **93**, 671.

28 (*a*) F. Shiraishi, T. Nakasako and Z. Hua, *J. Phys. Chem. A*, 2003, **107**, 11072; (*b*) E. R. Carraway, A. J. Hoffman and M. R. Hoffmann, *Environ. Sci. Technol.*, 1994, **28**, 786–793; (*c*) L. W. Miller, M. I. Tejedor and M. Anderson, *Environ. Sci. Technol.*, 1999, **33**, 2070–2075.

29 M. Schiavello, V. Augugliaro and L. Palmisano, *J. Catal.*, 1991, **127**, 332.

30 (*a*) C. Y. Wang, D. W. Bahnemann and J. K. Dohrmann, *Chem. Commun.*, 2000, 1539–1540; (*b*) C. Y. Wang, C. Böttcher, D. W. Bahnemann and J. K. Dohrmann, *J. Mater. Chem.*, 2003, **13**, 2322.

31 C. Wang, R. Pagel, D. W. Bahnemann and J. K. Dohrmann, *J. Phys. Chem. B*, 2004, **108**, 14082–14092.

32 J. Fan, S. W. Boettcher and G. D. Stucky, *Chem. Mater.*, 2006, **18**, 6391.

33 D. W. Bahnemann, A. Henglein, J. Lilie and L. Spanhel, *J. Phys. Chem.*, 1984, **88**, 709–711 .

34 S. J. Gregg and K. S. W. Sing, *Adsorption, Surface Area and Porosity*, Academic Press, London, 1997, pp. 111–194.

35 T. Nash, *Biochem. J.*, 1953, **55**, 416.

36 (*a*) N. Serpone and A. Salinaro, *Pure Appl. Chem.*, 1999, **71**, 303–320; (*b*) N. Serpone, R. Terzian, D. Lawless, P. Kennepohl and G. Sauve, *J. Photochem. Photobiol., A*, 1993, **73**, 11.

37 A. Salinaro, A. Emeline, H. Hidaka, V. K. Ryabchuk and N. Serpone, *Pure Appl. Chem.*, 1999, **71**, 321–335.

38 S. Mayavan, N. R. Choudhury and N. K. Dutta, *Adv. Mater.*, 2008, **1–6**, 9999.

39 Y. M. Liang, H. M. Zhang, Z. Q. Tian, X. B. Zhu, X. L. Wang and B. L. Yi, *J. Phys. Chem. B*, 2006, **110**, 7828.

40 R. Liu, Y. Ren, Y. Shi, F. Zhang, L. Zhang, B. Tu and D. Zhao, *Chem. Mater.*, 2008, **20**, 1140–1146.

41 A. Tonscheidt, P. L. Ryder, N. I. Jaeger and G. Schulz-Ekloff, *Surf. Sci.*, 1993, **281**, 51–61.

42 (*a*) D. Lawless, N. Serpone and D. Meisel, *J. Phys. Chem.*, 1991, **95**, 5166–5170; (*b*) S. Tojo, T. Tachikawa, M. Fujitsuka and T. Majim, *Chem. Phys. Lett.*, 2004, **384**, 312–316.

43 (*a*) H. Tang, K. Prasad, R. Sanjines, P. E. Schmid and F. Levy, *J. Appl. Phys.*, 1994, **75**, 2042; (*b*) T. Kawahara, Y. Konishi, H. Tada, N. Tohge, J. Nishii and S. Ito, *Angew. Chem., Int. Ed.*, 2002, **41**, 2811–2813.

44 R. I. Bickley, *J. Catal.*, 1973, **31**, 389.

45 D. C. Hurum, A. G. Agrios, K. A. Gray, T. Rajh and M. C. Thurnauer, *J. Phys. Chem. B*, 2003, **107**, 4545.

46 A. L. Linsebigler, G. Lu and J. T. Yates, *Chem. Rev.*, 1995, **95**, 735.

47 S. Yin, H. Hasegawa, D. Maeda, M. Ishitsuka and T. Sato, *J. Photochem. Photobiol., A*, 2004, **163**, 1.

48 (*a*) N. Lakshminarasimhan, E. Bae and W. Choi, *J. Phys. Chem. C*, 2007, **111**, 15244; (*b*) Y. Huang, W. Ho, S. Lee, L. Zhang, G. Li and J. C. Yu, *Langmuir*, 2008, **24**, 3510.

49 C.-Y. Wang, R. Pagel, J. K. Dohrmann and D. W. Bahnemann, *C. R. Chim.*, 2006, **9**, 761–773.